# Preliminary results from the 13.2m Yebes antenna after the VGOS update

P. de Vicente, J. González,
L. Barbas, B. Córdoba

Informe Técnico IT-CDT 2016-05

Los desarrollos descritos en este informe técnico han sido cofinanciados por el Programa Operativo Fondo Tecnológico FEDER de la UE bajo el convenio IGN-MINECO denominado “Radiotelescopio de VLBI geodésico y astrométrico para su integración en la red VGOS (VGOSYEBES)”

UNIÓN EUROPEA
FONDO
EUROPEO DE
DESARROLLO
REGIONAL
"Una manera de hacer Europa"

# Revision history

| Version | Date | Author | Updates |
|---|---|---|---|
| 1.0 | 06-03-2016 | authors | First draft |
| 1.1 | 20-12-2016 | P. de Vicente | Efficiency and SEFD sections rewrite |

# Contents

# 1 Introduction

The 13.2m antenna has been ovehauled for VLBI Global System (VGOS) operations and this report describes the first tests performed to check the outcome from these updates. The VGOS updates consisted in the installation of a new cladding of the main reflector structure, the installation of 4 new temperature sensors and a ventilation system at the back-structure of the main reflector, a new broadband receiver including a new optical fibre system and its connection to the IF system composed of 4 Up Down Converters (UDC) whose output is used to feed the two DBBC2 or the RDBEs at the backends room.

# 2 Slew times after the installation of the cladding

We have made a preliminary test to check the impact of the installation of the cladding in the movement of the telescope. The cladding has increased the weight of the antenna by approximately $2\%$. To compensate for the increase of weight, counterweights were installed in the movable head. All the cladding together with its supporting trusts and the counterweights ammount a total of 4 tons. The compensation works for elevation movements but no compensation is possible for azimuth movements. The inertia moment of the antenna has increased and as a consequence the stress on the motors and the power required to move the antenna increases.

According to de Vicente (2005), the antenna attains its maximum speed and acceleration above a given critical value given by:

$$\delta_{crt} = \frac{\pi}{2}\frac{V_{max}^2}{A_{max}}$$

where $V_{max}$ is the maximum speed (12°/s), and $A_{max}$ (6°/s) is the acceleration.

The maximum speed is 12°/s for azimuth and 6°/s for elevation and the maximum acceleration is 6°/s$^2$ and 3°/s$^2$. According to the previous values the critical distances are:

$$\delta_{crt}(az) = 37.7^\circ$$
$$\delta_{crt}(el) = 18.8^\circ$$

Figs. 1 and 2 show the velocity of the antenna while slewing for three different cases: when the separation is below the critical distance, at the critical distance and above the critical distance. The medium distance slewed in elevation is slightly larger than the critical distance. This is easily spotted by comparing the width of the peak in elevation and azimuth as a function of time in Fig. 1. According to the elevation plot in Fig. 2 the distance is 22° whereas it should be 18.8°.

Fig. 3 shows the behaviour of the antenna before and after the installation of the cladding. The curves have been shifted in time for an easy comparison. No significant changes can be seen between before and after the cladding and we conclude that the motors can handle the increase of weight without a penalty in the slew time.

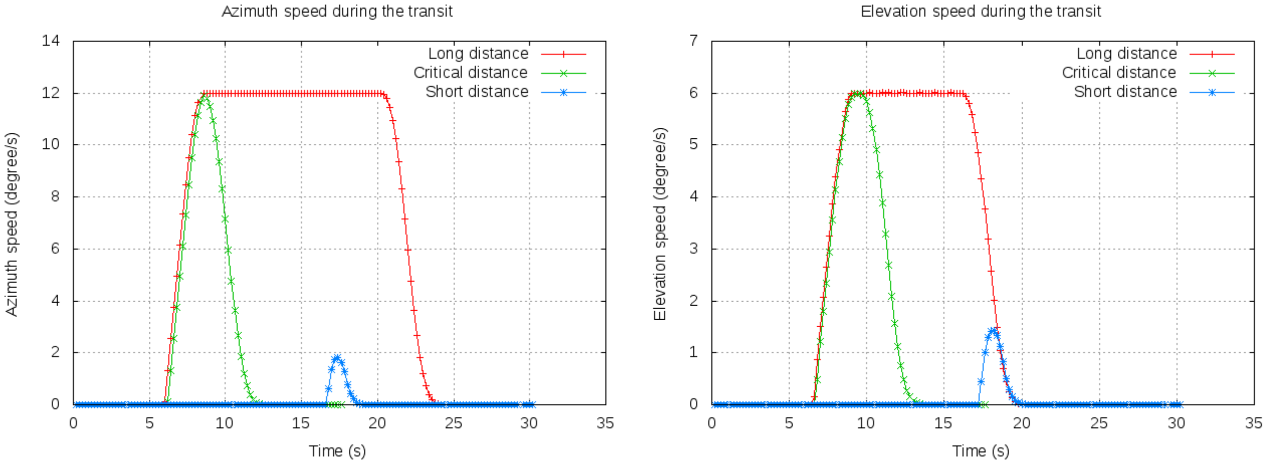

Figure 1: *Velocity of the antenna along azimuth and elevation between two points. Three cases can be distinguished according to the slew distance*

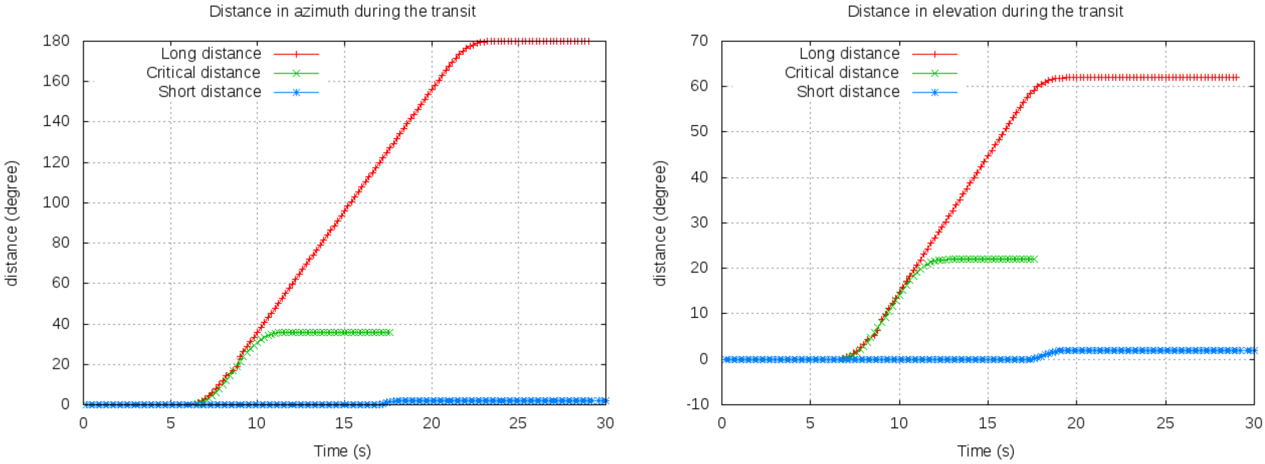

Figure 2: *Distance covered by the antenna during the slew movements for three different cases.*

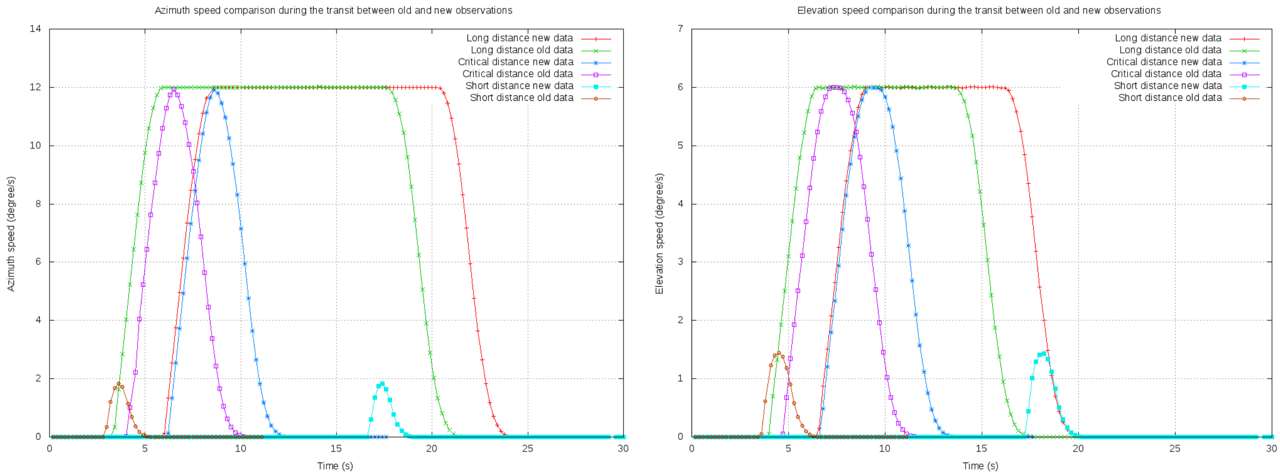

Figure 3: *Velocity of the antenna along azimuth and elevation axes between two points before and after the installation of the cladding. Three distances were tested.*

## 3 Temperature monitoring in the back-structure

The VGOS antenna has several temperature probes provided by MT-Mechatronics: two at the servo containers, one for the outdoor temperature attached to the container (Fig. 4), one at the azimuth cabin and four at the back-structure. Additionally the Observatory of Yebes provides weather parameters: temperature, pressure, humidity and wind information from a weather station, and the temperature and humidity at the elevation cabin.

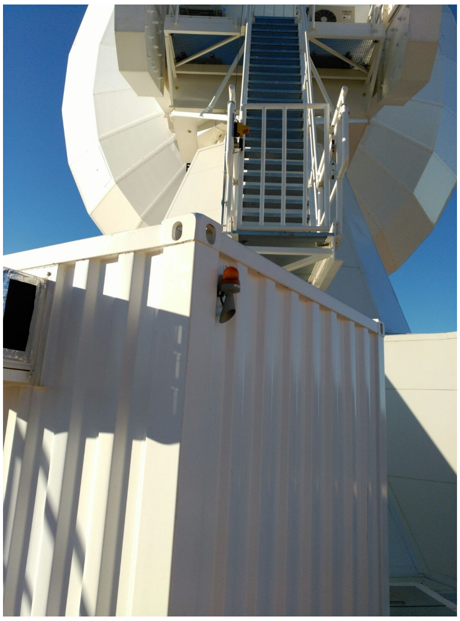

Figure 4: *Outdoor probe provided by MT-mechatronics. The face of the container shown in the picture looks towards the North - West*

Fig. 5 shows temperature measurements taken by the weather station and by the outdoor probe during approximately 22 hours. Temperatures between both probes are similar when the outside temperature, according to the weather station, is above 4 degrees. When the temperature is below that value the probes may show up to 2 degrees of difference, being the outdoor readout lower than the one from the weather station sensor.

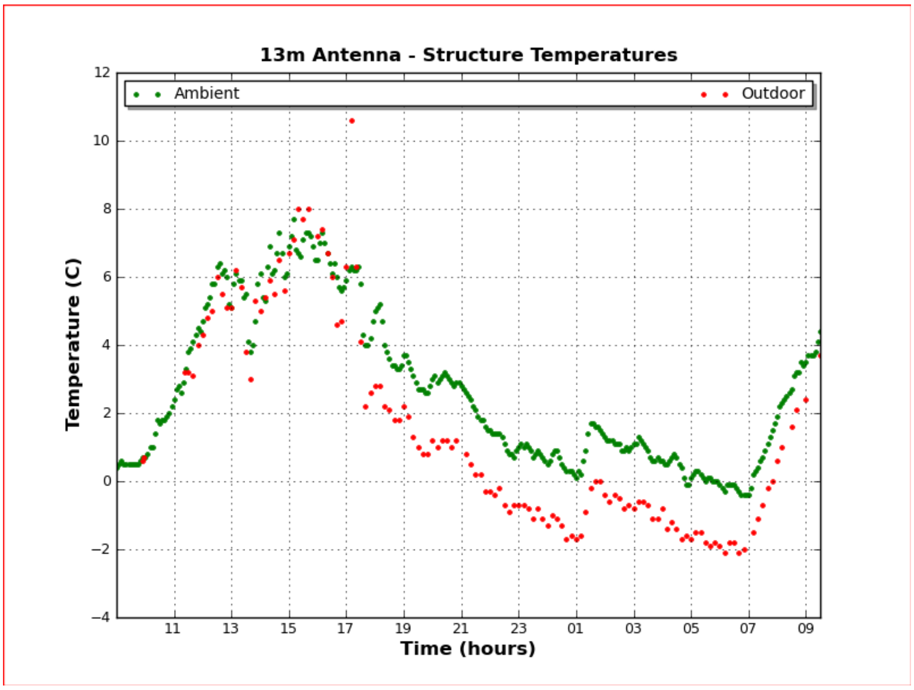

Figure 5: *Temperature values from the outdoor probe and the weather station temperature sensor. Data taken in March 2016*

The antenna software has been modified to retrieve the data from the new temperature sensors installed in the back-structure of the antenna. Fig. 6 shows the temperature along several hours together with the outside ambient temperature. The ventilation system, composed of 8 fans, forces air circulation in the back-structure and it is enabled every time the motors of the antenna are activated.

From the inspection of Fig. 6 some basic conclusions can be drawn:

1. The four sensors do not yield the same temperature. Differences among them may be up to 2 degrees. The largest difference is between probes 1 and 3, and the minimum between probes 2 and 4.
2. There is an inertia effect. The temperature inside the back-structure lags approximately 20 minutes from the outdoor temperature.
3. Apart from the inertia effect, the temperature readout from the sensors and the weather station may differ up to 2 degrees.

The difference between temperature sensors may have several causes:

- The sensors in the back-structure are not properly calibrated.

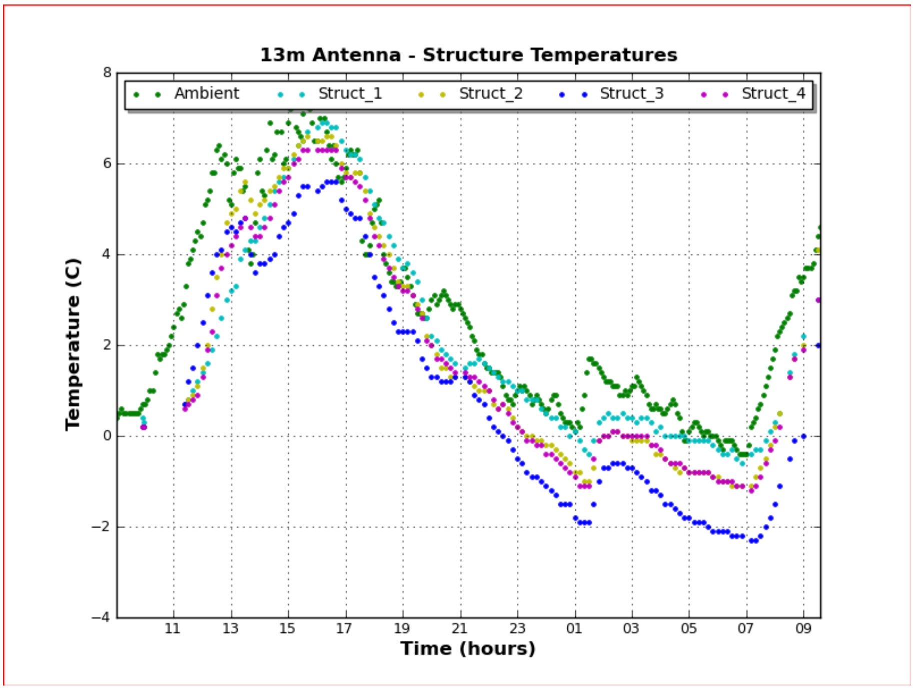

Figure 6: *Temperature values from 4 sensors located in the back-structure of the antenna, below the cladding. The outside ambient temperature from the weather station is also displaye for comparison.*

- There is a gradient of temperature across the structure which may arise from a non uniform exposition of the antenna to the sun. Measurements during the night discard this hypothesis since the irradiation should be uniform.

Unfortunately no sensors were installed before the cladding was set and no comparison with earlier dates is available.

# 4 Cabling at the backends room

The signal from the frontend, 2-14 GHz, is sent to the backends room at the 40m radiotelescope using two optical fibers out of a cable with 12 of them. Two optical transmitter-receiver units are installed at both ends, the 13.2m the elevation cabin and the backends room (García et al. 2016). The pair of transmitters, both from MITEQ are however different and have different gains: 16 dB (Digital Fiber Optic Transmitter/Receiver ) and 8 dB (SCMR Optical Fiber Transmitter/Receiver). The low gain fiber is connected to polarization V (optical patch cord 1 at the elevation cabin and R10) and the high gain to polarization H (optical patch cord 2 at the elevation cabin and R11).

The signals from the optical fiber receivers are fed into a divider that sends the signal to the four Up Down Converters (UDCs). The UDCs are installed at the backends room. Each UDC has 2 outputs in two different polarizations and therefore there are 4 outputs with horizontal polarization (coded H) and four outputs with vertical polarization (coded V). Each output has a copy that may be used for any other purpose.

## 4.1 Cabling until June 2016

Fig. 7 shows the cabling used at the backends room for some tests described in this report. The UDC H outputs were injected into DBBC2 1 and the V outputs into DBBC2 2 input IFs. For continuum pointing drifts we used two types of outputs from each IF of the DBBC: a copy of the input (tagged as OUT) and a filtered copy of the input (tagged as MON). These outputs were connected to the input of the IRAM Detector, coded internally as IDET, and to a Keysight Power Meter with two channels, coded locally as POWM respectively.

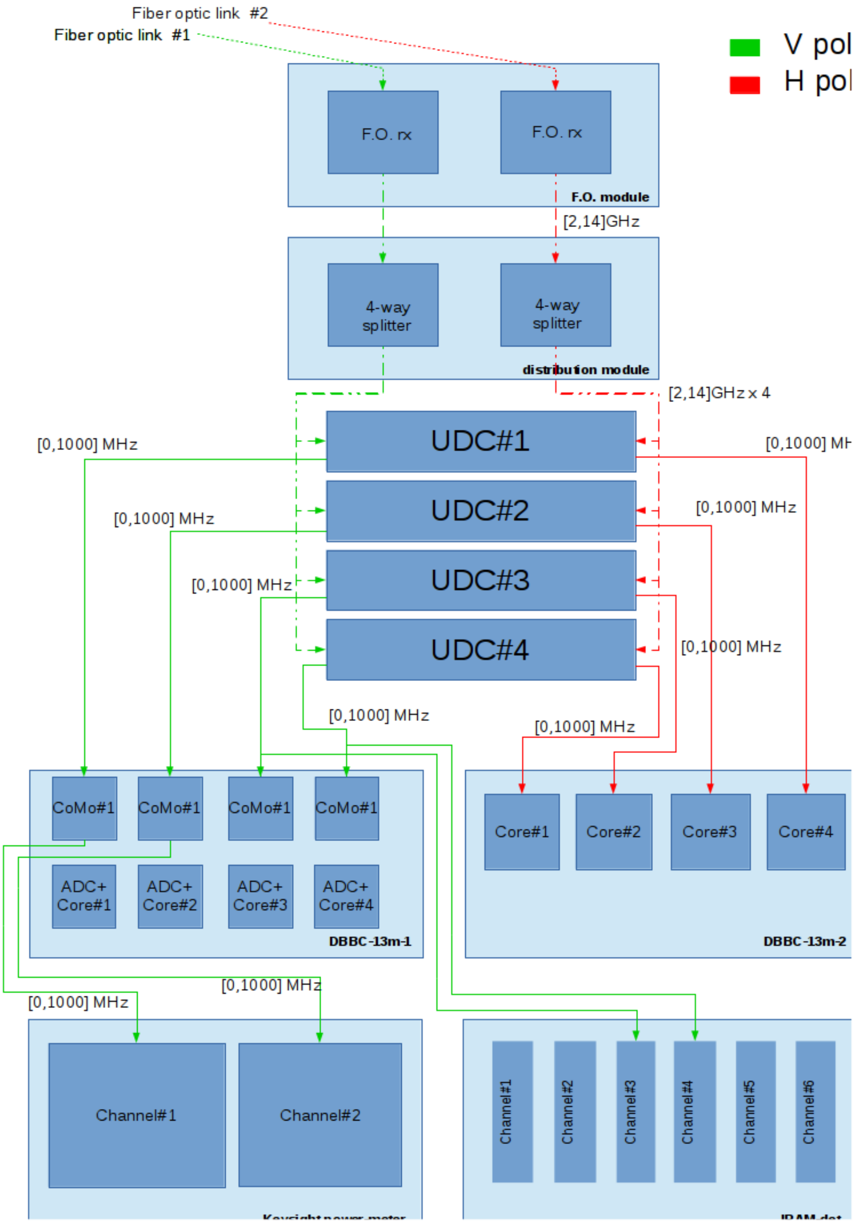

Figure 7: *Cabling at the backends room for the tests described in this report.*

The DBBcs were configured to use a filter of 1 GHz, option 6 in the Field System, and to disable the Auto Gain Control (AGC) to guarantee that all measurements were done with the same gain along the receiving chain. We have connected all main outputs from the UDCs to IF input 2 of each DBBC. The control of the DBBCs (input, gain and filter) was automatically done from the 13m VGOS antenna control system. To measure the zero of the continuum detectors the remote control system sets the input of the DBBC IFs to its 4th entry which is connected to a 50 Ohm load.

### 4.2 Cabling between June and November 2016

During this period we used a hybrid system composed of two or one DBBCs and one or two RDBEs. In this case we kept all connections to the DBBCs and used the copy outputs from the UDCs to inject the signal into the RDBEs. To avoid passing through the DBBCs to make continuum observations we have connected both monitor outputs from UDC2 into 5 and 6 inputs of the continuum IramDetector backend.

### 4.3 Cabling after December 2016

In late November 2016 four RDBEG units were installed at the backends room. The final setup is depicted in Fig. 8. The monitor signal from UDC 2 is connected to inputs 5 and 6 at the IramDetector. It is also possible to use the RDBEs as continuum detectors taking advantage of the multicast with a rate of 1 Hz. In principle, with this option no continuum detector would be required.

The setup with the four RDBEG units is not the definitive one since they do not comply with the full VGOS specification: they provide 500 MHz bandwidth and a data rate of 2 Gbps, whereas they should cover 1 GHz bandwidth with a recording rate of 4 Gbps per unit (2 channels). It is still to be decided if to use the third generation of RDBEs or a DBBC3 fully VGOS compliant.

## 5 First observations

We present the first single dish observations with the 13.2m VGOS antenna. The observations consisted in pointing drifts along the azimuth and elevation axes towards Cas-A, a supernova remnant. This source is intense and its size is lower than the beam of the telescope at frequencies below 14 GHz.

The first series of observations was uncalibrated because the calibration system was still under tests. No focus optimization was performed but the focus position determined with the triband receiver was used. In order to test the four UDCs, observations at different frequencies and with different units were done. Results at 7.5 GHz are displayed on Fig. 9. Appendix 1 contains a number of drifts at other frequencies in Figs. 19 to 28.

The first observations showed, in some cases, some lack of repetivity in the pointings for each frequency and different UDCs which we believe was caused by RFI. Further observations have been done through the last months to get a pointing model and a better focusing. These

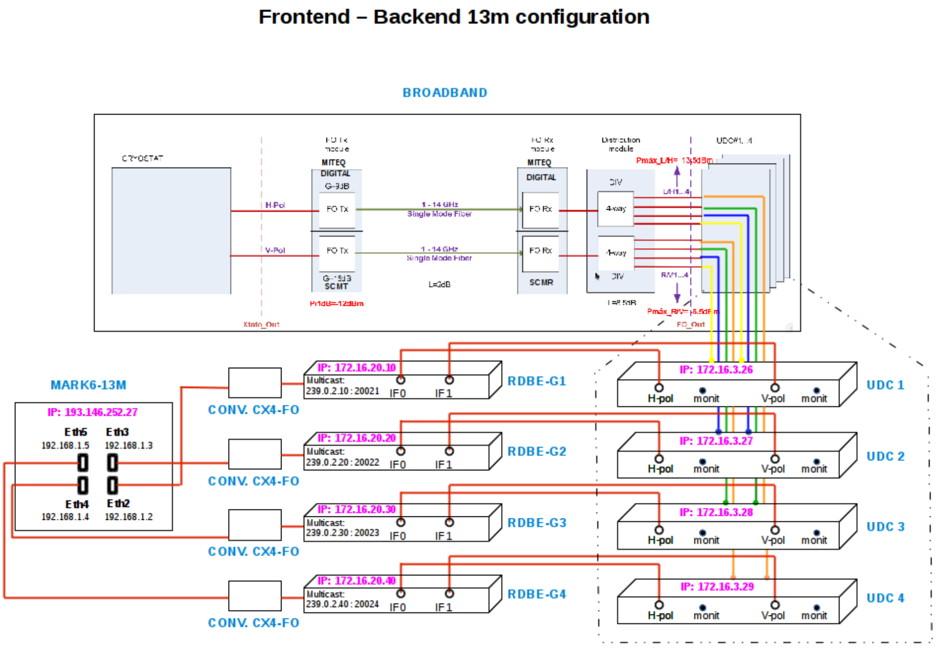

Figure 8: *Cabling at the backends room using 4 RDBEG units for VLBI*

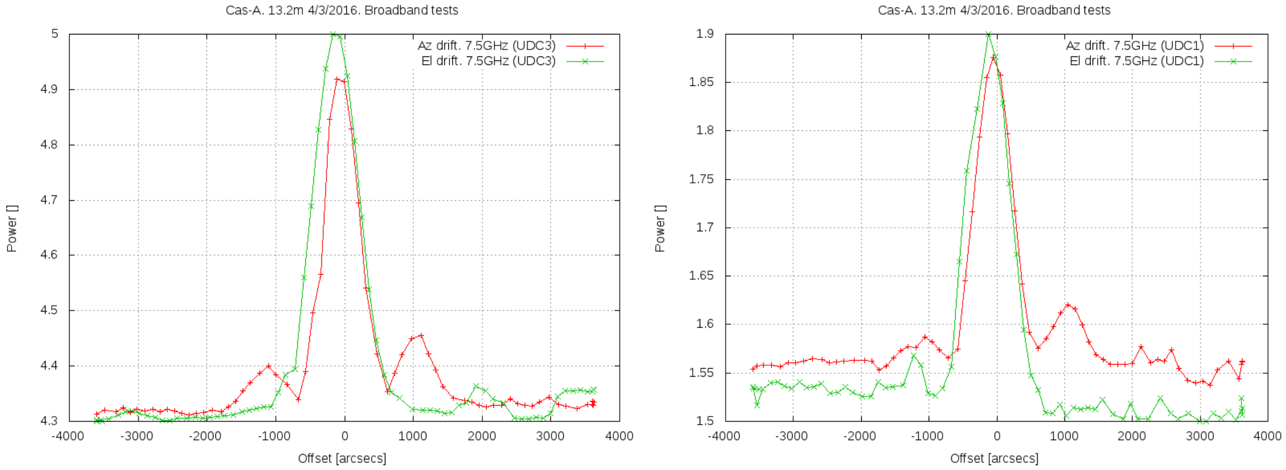

Figure 9: *Pointing drifts at 7.5 GHz towards Cas-A with vertical polarization*

first observations were taken with the Keysight Power Meter in fast mode (200 samples per second) and with a total integration time of 1 second. The fast mode allowed to minimize the time between integration samples to 5 milliseconds.

To compare with current results we show a similar pointing drift at 7.5 GHz this time calibrated.

# 6 RFI

Radio Frequency Interference (RFI) in the Observatory environment has been studied by Cordobés and López-Pérez (2016). In this section we present the result of integrating all the detected emission between 2 and 6 GHz using a continuum detector equipped with two heads. The integration time was set to 1 second. The continuum detector was directly connected to the output of the frontend. Fig.10a shows the power detected at 3 different elevation angles as a function of azimuth. High power is coming from several azimuth directions probably associated to towns and cities around the observatory.

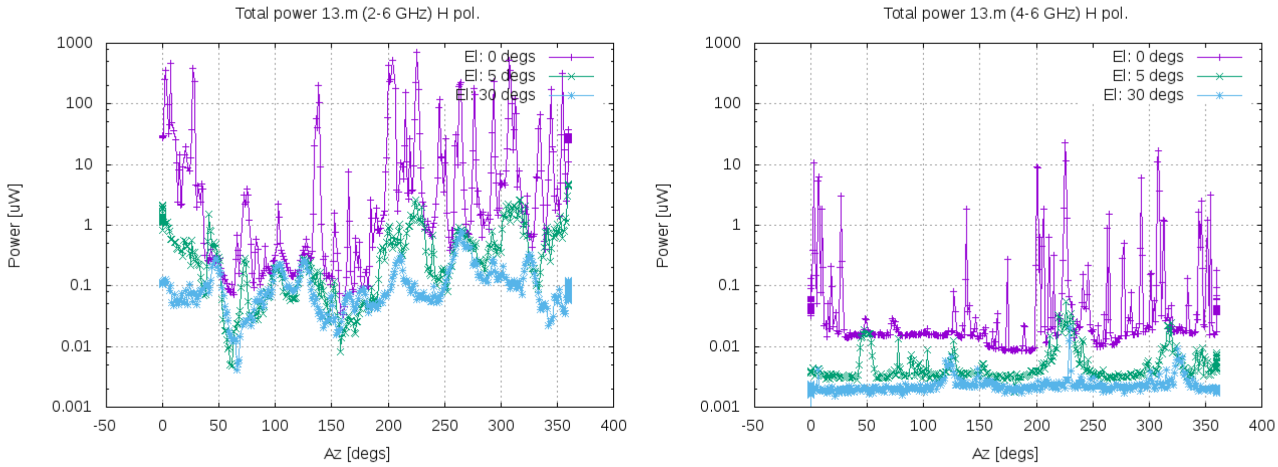

Figure 10: *Three 360° azimuth drifts at 0, 5 and 30 degrees elevation. a) Left panel: total power between 2 and 6 GHz. b) Right panel: total power between 4 and 6 GHz. The peaks determine from which azimuth angles the RFI comes from.*

We repeated these observations using a filter that blocks all power below 4 GHz and the result is in Fig. 10b. For higher frequencies the status is much better, specially at elevations above 5 degrees elevation. As seen from Fig. 10 observations starting at 2 GHz are plagued with RFI at almost any direction, whereas at frequencies above 4 GHz the RFI is almost non existent above 5 degrees elevation.

We have also measured the total power at different directions from the sky and represented the values as a function of elevation. Fig. 11a shows the results when using a detector between 2 and 6 GHz. The form of the curve is very peculiar and different from a standard namsyth telescope. We believe that the shape we see, having a minimum at 30 degrees and an increase towards 90 degrees where it attains its maximum, as with very low elevations, is due to the ring focus subreflector. This type of subreflector has a sharp edge in the center that picks up radiation from the ground (RFI or thermal) increasing the detected power. Fig. 11b shows the same results as in panel b, but radiation between 2 and 4 GHz was filtered out. Fig. 11a shows that possibly, in no case we see thermal noise, but RFI.

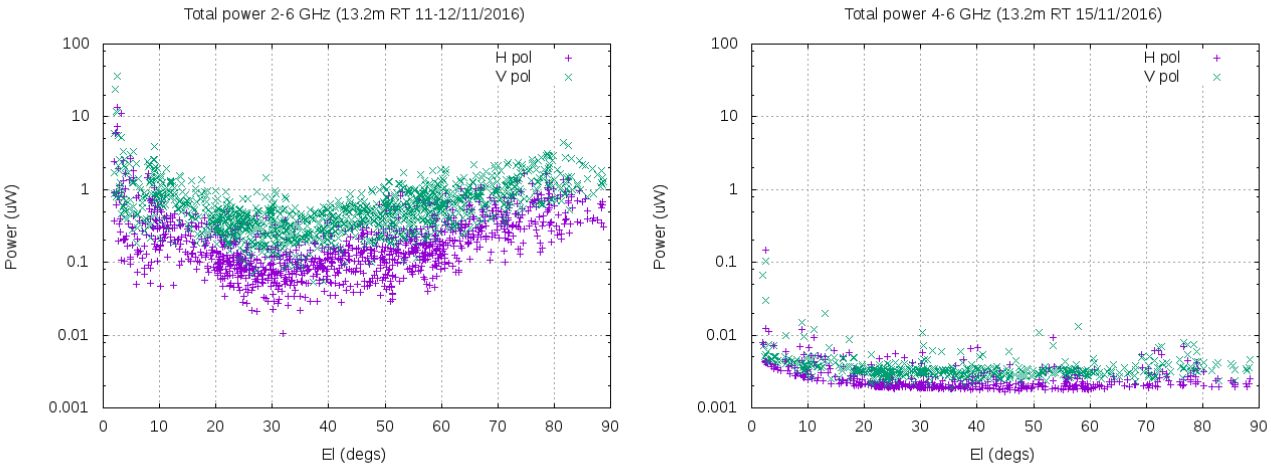

Figure 11: *Total power versus elevation for many different azimuths. a) Left panel: total power between 2 and 6 GHz. b) Right panel: total power between 4 and 6 GHz.*

We conclude that Yebes Observatory suffers severe RFI at frequencies below 4 GHz and this should be taken into account in the design of the RF and IF chain. The ring focus subreflector worsens this situation at higher elevations.

# 7 The calibration diode

The broadband receiver injects the noise from a noise diode along the band. It can work in a single shot mode or driven by an 80 Hz periodic signal. Fig. 12 shows a typical calibration scan showing five phases: off the source and noise diode off, off the source and noise diode on, on the source and noise diode on, on the source and noise diode off, and zero offset. On the second phase, when the noise diode is switched on, the voltage overshoots on ocassions and later it gets down to a stable lower value. To avoid this artificial value when computing the system temperature, the software uses the second sample from each subscan of a calibration scan to determine its voltage.

The continuous calibration at 80 Hz has been tested and compared with single shot calibration. Tsys with both systems differs 1% at most and therefore we assume that driving the noise diode at 80 Hz does not affect its power level. Synchronous detection is possible with both the RDBE and the DBBC. Each RDBE generates an 80 Hz square signal, such that the rising edge is synchronized with the rising edge of the local station PPS. This implementation guarantees that all RDBEs can detect the square signal synchronously, even if the signal is driven only by one of the RDBEs. Currently the 80 Hz from RDBE for band D is the one used for driving the noise diode at the receiver. The cal diode temperature used across the band is shown in Fig. 13.

The DBBC is also syncronized with the PPS, but in this case the decreasing edge of the 80 Hz signal is synchronized with the rising edge of the PPS. It is possible to change the polarity

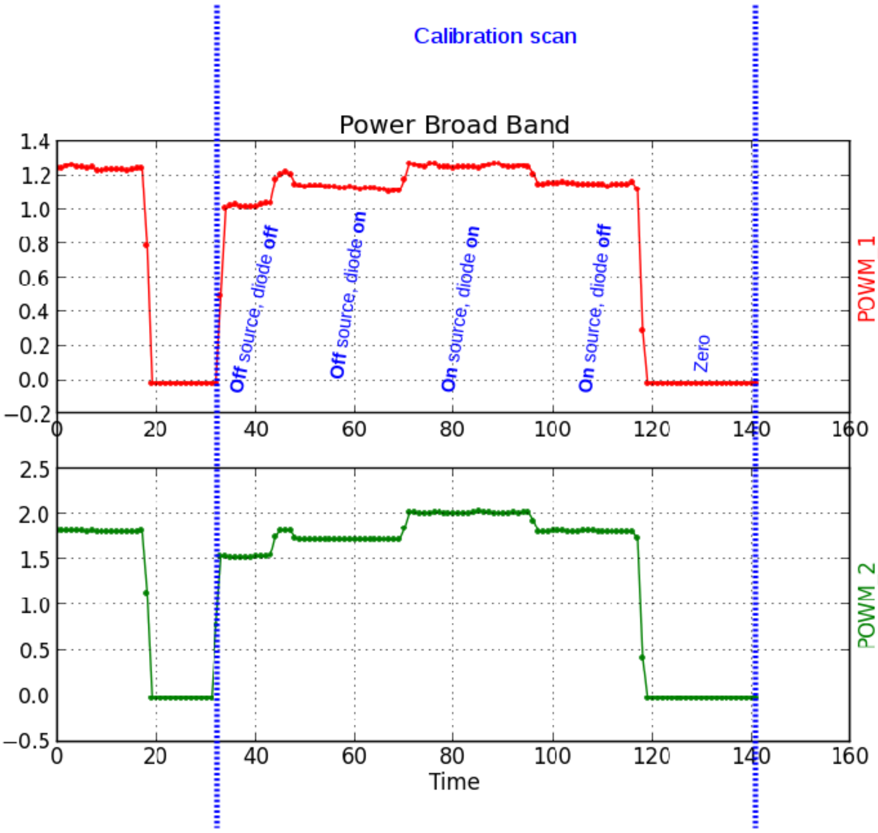

Figure 12: *Typical calibration scan composed of five phases. The second phase, when the diode is switched on, shows an overshoot that should be disregarded*

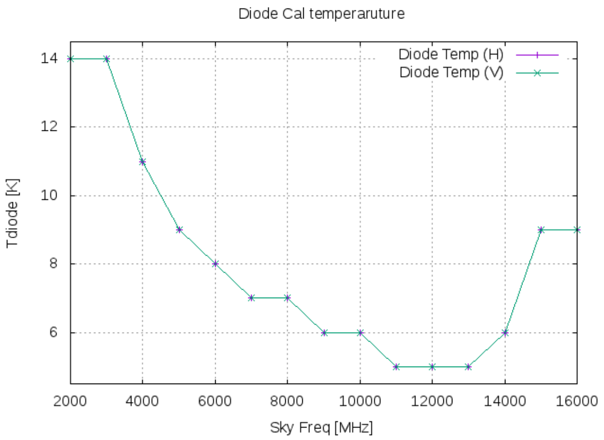

Figure 13: *Cal diode temperature as function of frequency. Values delivered by Yebes receiver laboratory.*

with a remote command available both for PFB and DDC modes.

# 8 System temperature

We measured the system temperature using the 32 MHz channels from one RDBE backend and continuous switched calibration at 80 Hz. The antenna was ponting towards an elevation of 68 degrees and an azimuth of 250 degrees. The measurement was done with a 3.5 GHz high pass filter and hence no values are provided below that frequency. The result is shown in Fig. 14. Data between 5.5 and 6.5 GHz are missing due to an error in the measuring procedure.

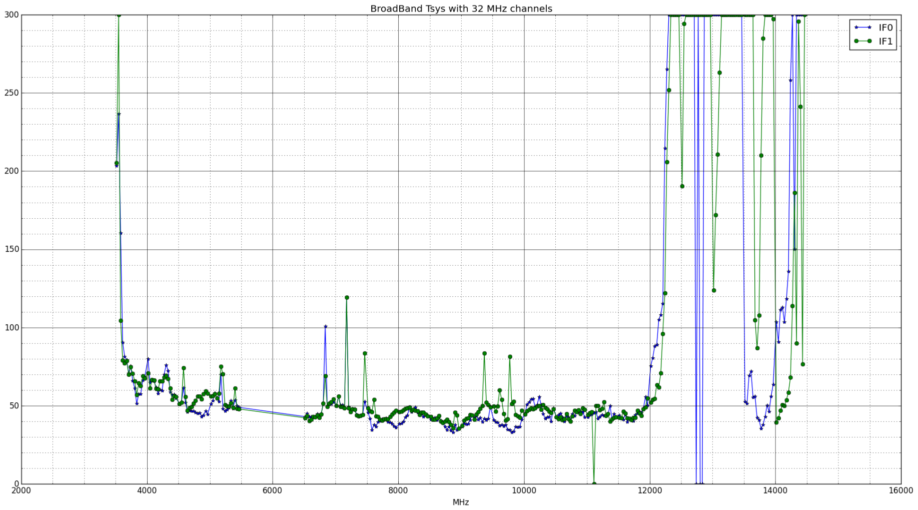

Figure 14: *Tsys obtained using 32 MHz bandwidth detectors from the RDBE in continuous cal mode. IF0 was connected to horizontal polarization and IF1 to vertical polarization*

The system temperature is below 50 K between 6.5 and 12 GHz and below 70 K between 3.5 and 5.5 GHz. Above 12 GHz the values are extremely high and at the time of this report we have not investigated the cause for these behaviour.

# 9 Aperture efficiency

The aperture efficiency has been estimated from observations towards Taurus A and Cassiopea A, two sources of well known flux. These sources are quite convenient at centimeter wavelenghts for small antennas. An updated review on calibrator sources is available by Perley and Butler (2016) but since it has a limited frequency range, in particular for Tau A and Cas A, we have not used it here. Instead we have used the values by Baars (1977) and applied a decreasing flux correction factor for Cas A.

The efficiency can be estimated, according to Baars, as:

$$\eta_a = \frac{2K_B C_s T'_a}{A S_f} \tag{1}$$

where $T'_a$ is the antenna temperature corrected by the atmospheric attenuation, $A$ the radiotelescope collecting area, $S_f$ the source flux and $C_s$ a factor which takes into account the source brightness distribution compared to the antenna HPBW and it is only valid for sources whose size is equal or smaller than the beam width:

$$C_s = \begin{cases} 1 + x^2 & \text{gaussian source} \\ \frac{x^2}{1-\exp(-x^2)} & \text{disk source} \end{cases} \tag{2}$$

where,

$$x = \frac{\theta_s('')}{1.2\,\theta_b('')} \tag{3}$$

and $\theta_s$ is the source size and $\theta_b$ the HPBW of the antenna.

For the 13.2 m radiotelescope we can write:

$$\eta_a = 20.168 \frac{C_s\, T'_a[\text{K}]}{S_f[\text{Jy}]} \tag{4}$$

Table 10 summarizes the efficiency and the parameters used for computing it from observations towards both sources. We assumed a source size of 300 arcsecs and a gaussian shape geometry for Tau A and a size of 240”, a disk shape geometry and a decreasing flux for Cas A. The antenna temperature was determined using a noise diode calibrator whose value was calibrated previously at the laboratory.

Taurus A and Cassiopea fluxes were estimated from this expression:

$$\log S = a_0 + a_1 \log(\nu) + a_2 \left[\log(\nu)\right]^2 \tag{5}$$

where the coefficients for Taurus A and Cassiopea A are summarized in Table 9. Cassiopea A flux decreases with time and according to Baars (1977) the flux is computed as follows:

$$S = S_{1980} \left[ 1 - (Y - 1980) \frac{(0.97 - 0.30 \log(\nu))}{100} \right] \tag{6}$$

where $S_{1980}$ is the flux of the source in 1980, $\nu$ the observing frequency in GHz and $Y$ is the current year.

Fig. 15 shows the aperture efficiency as a function of elevation for Cas A and Tau A at 3 different sky frequencies: 6.5, 9.5 and 12.5 GHz. A continuum detector with 1 GHz bandwidth was used.

According to Fig. 15 the efficiency drops with elevation by 10% at 70 degrees with respect to 10 degrees elevation. The efficiency also drops with frequency. Fig. 29 shows the aperture efficiency as a function of frequency, where each point has been obtained by averaging all points at a given frequency and for all elevations.

| Source | $a_0$ | $a_1$ | $a_2$ |
|---|---|---|---|
| Tau A | 3.915 | -0.299 | 0 |
| Cas A | 5.745 | -0.770 | 0 |

Table 1: *Coefficients for fitting equation 5 to obtain the flux for some calibrators. Obtained from Baars (1977). Cas A flux is for year 1980.*

| Frequency | Tau A | | | Cas A | | |
|---|---|---|---|---|---|---|
| [MHz] | Flux density [Jy] | Cs | $\eta_a$ | Flux density [Jy] | Cs | $\eta_a$ |
| 3500 | 717 | 1.04 | | 727 | 1.0 | |
| 4500 | 664 | 1.06 | | 610 | 1.0 | |
| 5500 | 626 | 1.12 | 0.60 | 529 | 1.0 | 0.66 |
| 6500 | 595 | 1.17 | 0.61 | 471 | 1.0 | 0.63 |
| 7500 | 570 | 1.23 | 0.59 | 426 | 1.0 | 0.58 |
| 8500 | 549 | 1.30 | 0.60 | 390 | 1.0 | 0.58 |
| 9500 | 531 | 1.37 | 0.58 | 360 | 1.01 | 0.51 |
| 10500 | 516 | 1.45 | 0.62 | 335 | 1.02 | 0.53 |
| 11500 | 500 | 1.54 | 0.52 | 314 | 1.03 | 0.43 |
| 12500 | 490 | 1.64 | 0.53 | 297 | 1.04 | 0.41 |
| 13500 | 479 | 1.74 | 0.54 | 281 | 1.05 | 0.44 |

Table 2: *Flux and aperture efficiencies computed for different frequencies from Tau A observations. RFI at low frequencies prevents a reliable Ta* determination*

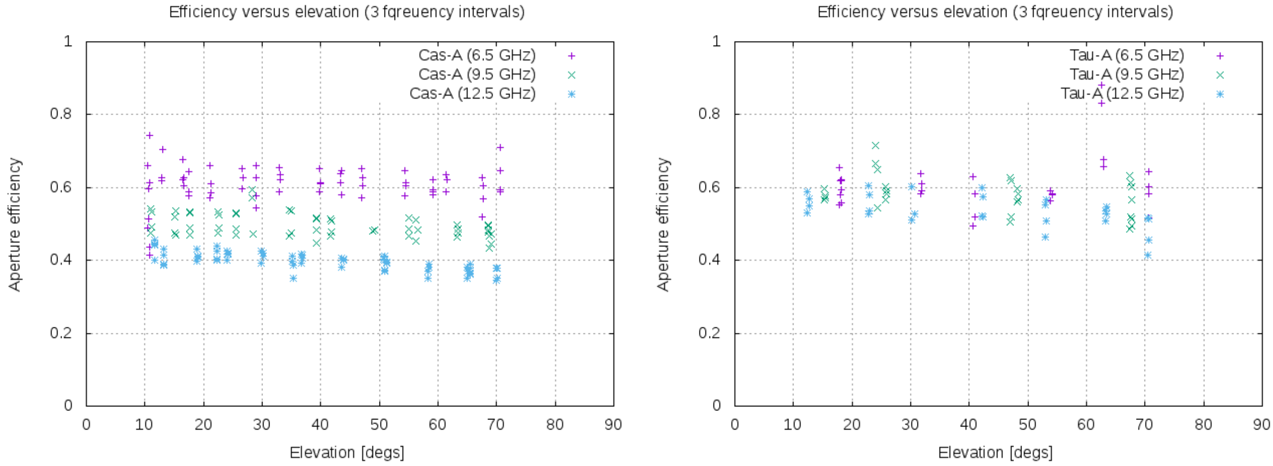

Figure 15: *Aperture efficiency at 6.5 GHz, 9.5 GHz and 12.5 GHz obtained observing Cas A and Tau A using a total power detector with 1 GHz bandwidth.*

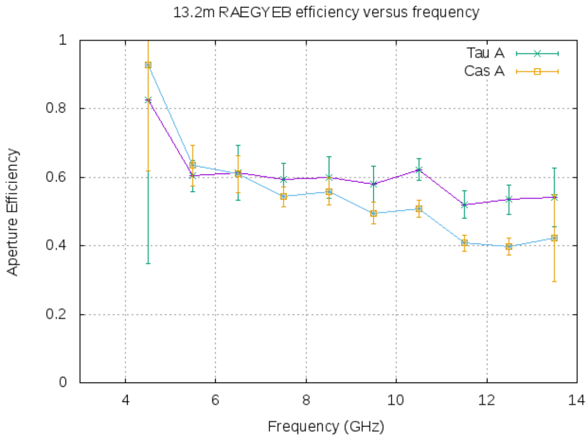

Figure 16: *Aperture efficiency as a function of frequency. Each point has been obtained averaging the measurements at all elevations and with a bandwidth of 1 GHz.*

# 10 SEFD and G/T. Onoff observations

We performed an initial estimation of the Source Equivalent Flux Density at different frequencies observing towards Cas A and Tau A. This estimation can be done without a previous calibration, if we determine the ratio between the power of the signal due to the source (once we substract the emission from the background and correct for atmospheric opacity) versus the power towards the sky and the known flux of the astronomical source. Care should be taken since the size of the source compared to the beam size should be considered in the estimation:

$$SEFD = S_f \frac{T_{sys}}{Ta'} C_s \tag{7}$$

Fig. 17 summarizes the results obtained from Cas A and Tau A between 3.5 and 13.5 GHz. The data were obtained using the same procedure as in the previous section with 1 GHz bandwidth continuum backend. The SEFD has been computed separately for the horizontal and the vertical polarization since the system temperature differs for both polarizations. The SEFD is worse for the vertical polarization than for the horizontal because of the different system temperatures. Higher system temperatures and a slightly lower efficiency are the cause for SEFD increases at the upper end of the frequencies. The lower end is affected by RFI. In the mid-term future RFI filters will be installed together with low noise amplifiers before the optical fibre system which will improve the SEFD.

G/T (Gain over Temperature) is a figure similar to the Source Equivalent Flux Density (SEFD) used in engineering environments. We include it here because it is a preliminary measurement which, as with the SEFD, does not require calibration and helps estimating quickly the performance of the telescope. It involves calculating the ratio of power between two different positions: the source and the sky close enough to get the same contribution from the atmosphere but not from the source.

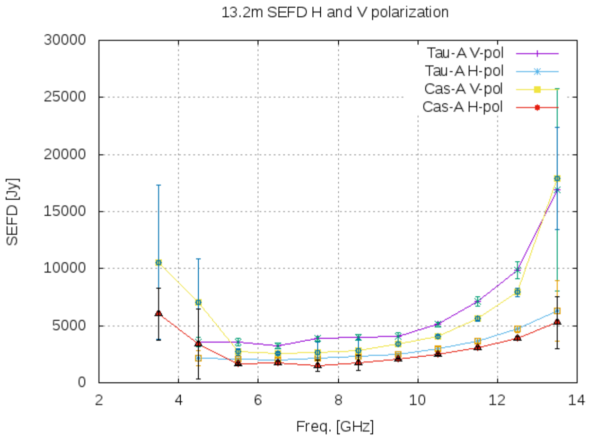

Figure 17: *SEFD (Jy) for the horizontal and vertical polarizations obtained from Tau A and Cas A and using a continuum detector 1 GHz bandwidth.*

Then G/T is defined as:

$$G/T = \frac{8\pi k(Y-1)}{S\lambda^2}K_1K_2$$

where $k$ is the Boltzmann constant, $Y$ is the ratio of power between the source and the sky, always larger than 1, $\lambda$, the wavelength of the radiation, $K_1$ is a correction for atmospheric attenuation and $K_2$ correction for the size and shape of the source, and it may be considered the same as $C_s^{-1}$ defined above, and where

$$Y = \frac{V_{source}}{V_{sky}}$$

Units for G/T are dB over K.

The relationship between SEFD and G/T is obtained by taking into account that:

$$Y = \frac{V_{source}}{V_{sky}} = \frac{S_f}{SEFD}C_s + 1$$

and hence we have:

$$G/T = \frac{8\pi k}{SEFD\lambda^2}K_1$$

Table 10 summarizes the results obtained from observations towards Cas-A sorted by frequency.

# 11 Beam pattern

We have measured the beam of the telescope at different frequencies drifting on top of a source. The results are unusal and require further investigation. See Fig. 18 for an example. We

| **Frequency** | | **Tau A** | | | **Cas A** | |
|---|---|---|---|---|---|---|
| | SEFD V | SEFD H | G/T | SEFD V | SEFD H | G/T |
| [MHz] | [Jy] | [Jy] | [dB/K] | [Jy] | [Jy] | [dB/K] |
| 3500 | | | | 10500 | 6000 | 29.0 |
| 4500 | 3550 | 2200 | 35.5 | 7000 | 3400 | 33.6 |
| 5500 | 3600 | 2100 | 37.5 | 2700 | 1600 | 38.5 |
| 6500 | 3200 | 2000 | 39.1 | 2500 | 1700 | 39.7 |
| 7500 | 3900 | 2200 | 40.0 | 2600 | 1500 | 41.6 |
| 8500 | 4000 | 2300 | 40.7 | 2800 | 1800 | 42.0 |
| 9500 | 4000 | 2500 | 41.4 | 3400 | 2100 | 42.2 |
| 10500 | 5100 | 3000 | 41.6 | 4000 | 2500 | 42.3 |
| 11500 | 7100 | 3700 | 41.4 | 5600 | 3000 | 42.2 |
| 12500 | 9900 | 4700 | 41.1 | 7900 | 3900 | 41.9 |
| 13500 | 17000 | 6300 | 40.0 | 17900 | 5300 | 41.2 |

Table 3: *SEFD and G/T values for different frequencies from Tau A and Cas A observations. RFI at low frequencies prevents a reliable estimation of both parameters. SEFD values have been rounded to multiples of 100 due to the RMS error. G/T values have been computed only for the horizontal polarization.*

used the continuum backend IramDetector with a bandwidth of 1 GHz and two simultaneous frequencies: 6.5 and 10.5 GHz towards Cassiopea A.

Fig. 18 shows different shapes which depend on the polarization used to detect the data: the horizontal polarization for azimuth drifts shows a gaussian shape beam pattern, whereas elevation drifts show secondary lobes. The opposite happens when doing elevation drifts: if the polarization is horizontal the shape shows secondary lobes and the vertical polarization shows a gaussian shape. In summary: when the linear polarization matches the direction of the drift the beam pattern shows a gaussian shape whereas in the other cases, polarization is 90 degrees with respect to the drift, the beam shape shows secondary lobes.

The secondary lobes show a level of approximately 15% (8 dB) of the main peak. The behaviour described above is independent of the observing frequency

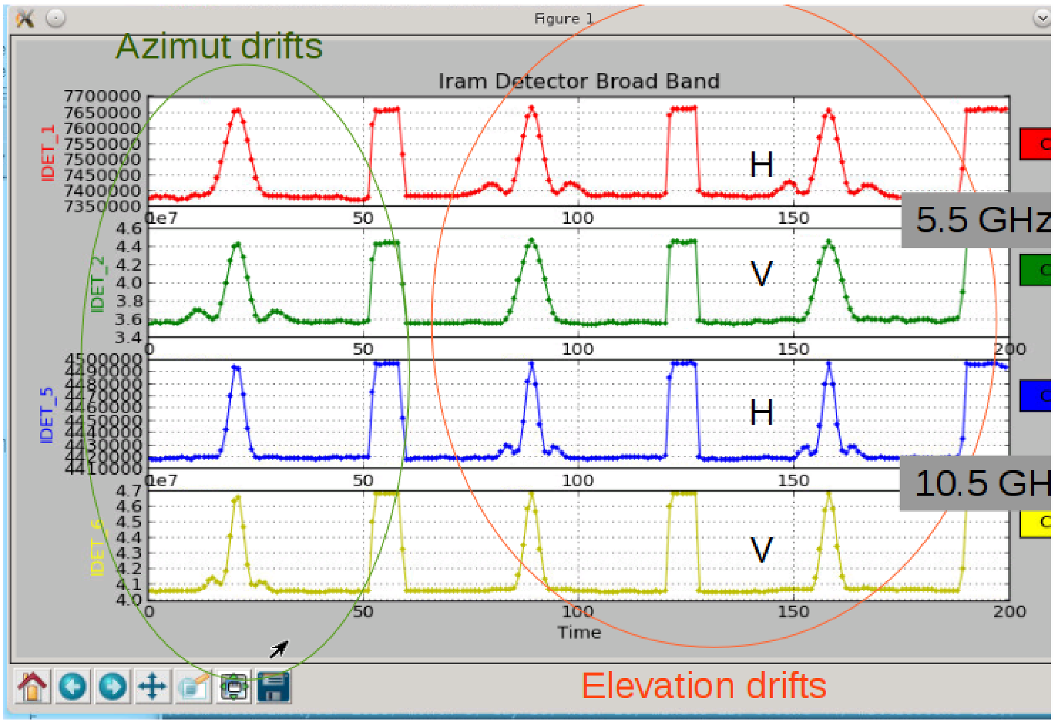

Figure 18: *Detected voltage as a function of time at 6.5 and 10.5 GHz for an azimuth drift followed by an elevation one.*

# 12 Appendix 1. First pointing drifts

We include in this section the first drifts done at different observing frequencies between 3.5 and 13.5 GHz in steps of 1 GHz towards Cas A. The IramDetector continuum backend was used providing 1 GHz detection bandwidth. All drifts are uncalibrated and are included as a historical document of the first measurements performed with the broadband receiver. After these observations the backend was modified to have 1 GHz bandwidth.

# 13 Appendix 2. Aperture efficiency

Estimation of the aperture efficiency as a function of elevation for different sky frequencies using two sources: Cas A and Tau A. Each frequency data was obtained with a continuum detector 1 GHz bandwidth.

# References

[1] Baars, J. W. M., Genzel, R., Pauliny-Toth, I. I. K., Witzel, A. Astronomy and Astrophysics, vol. 61, no. 1, Oct. 1977.

[2] Cordobés D., López-Pérez J.A. Second radio-frequency interference measurement campaign at Yebes observatory. Informe Técnico CDT 2016-8

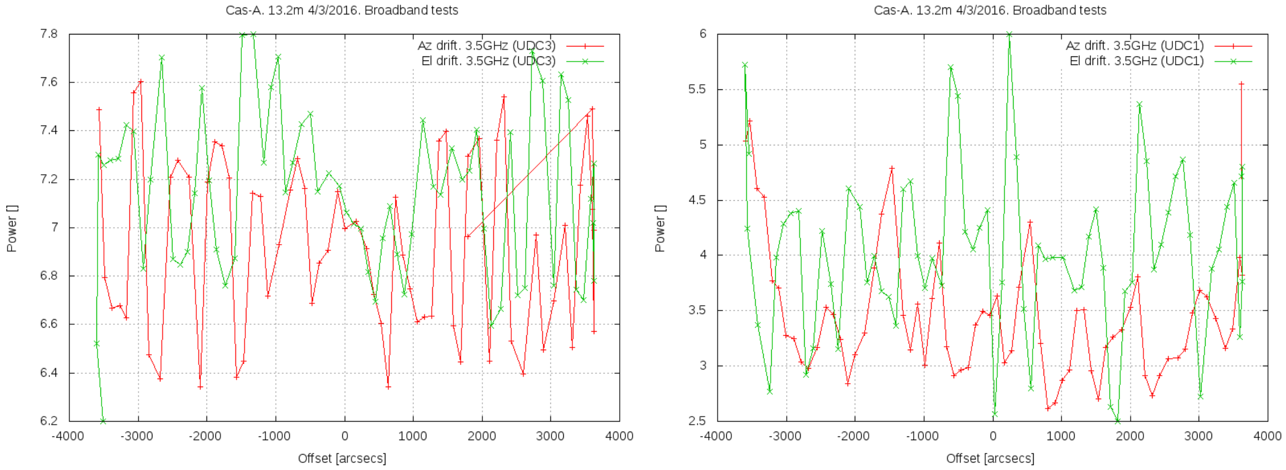

Figure 19: *Pointing drifts at 3.5 GHz towards Cas-A*

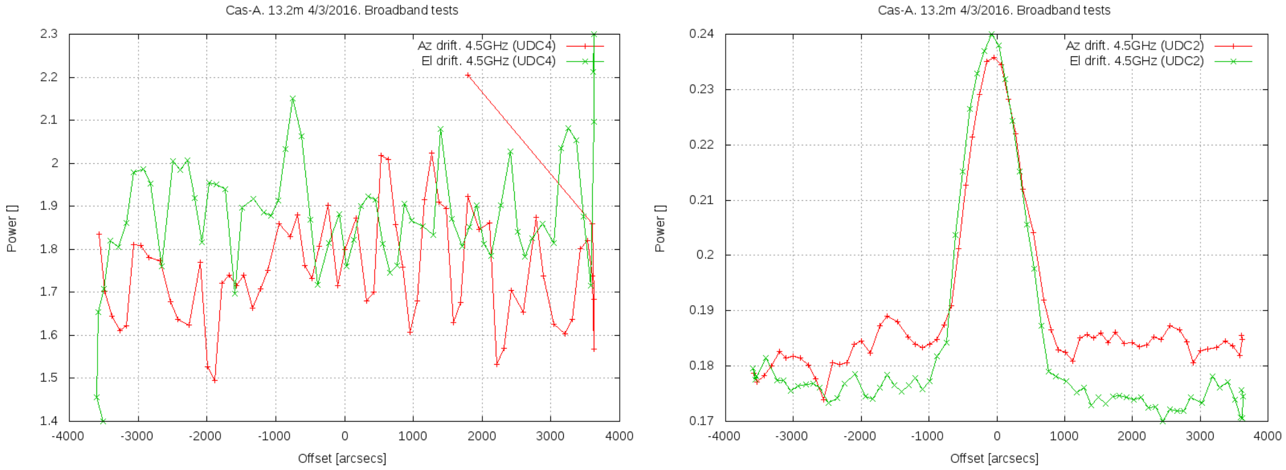

Figure 20: *Pointing drifts at 4.5 GHz towards Cas-A*

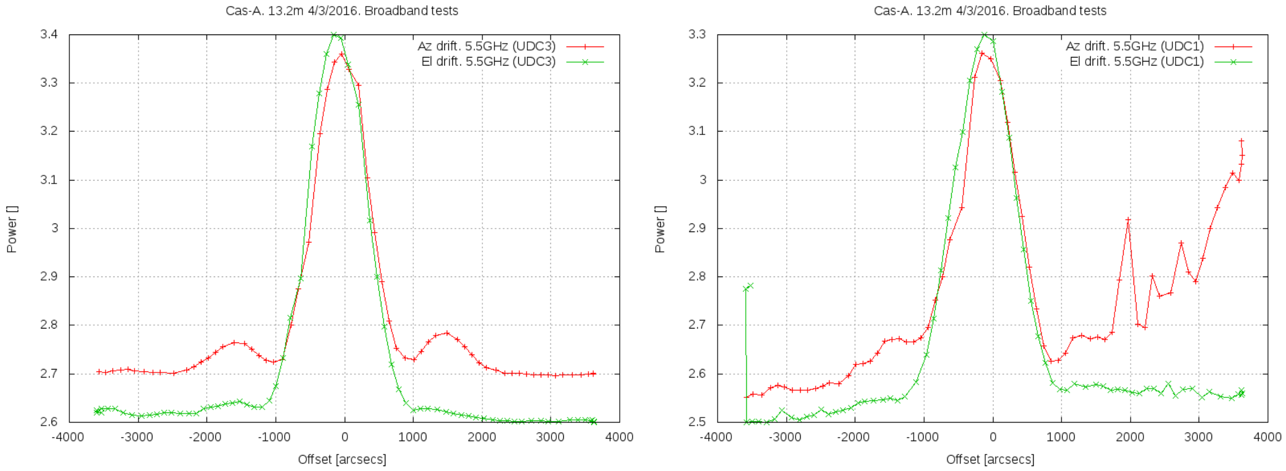

Figure 21: *Pointing drifts at 5.5 GHz towards Cas-A*

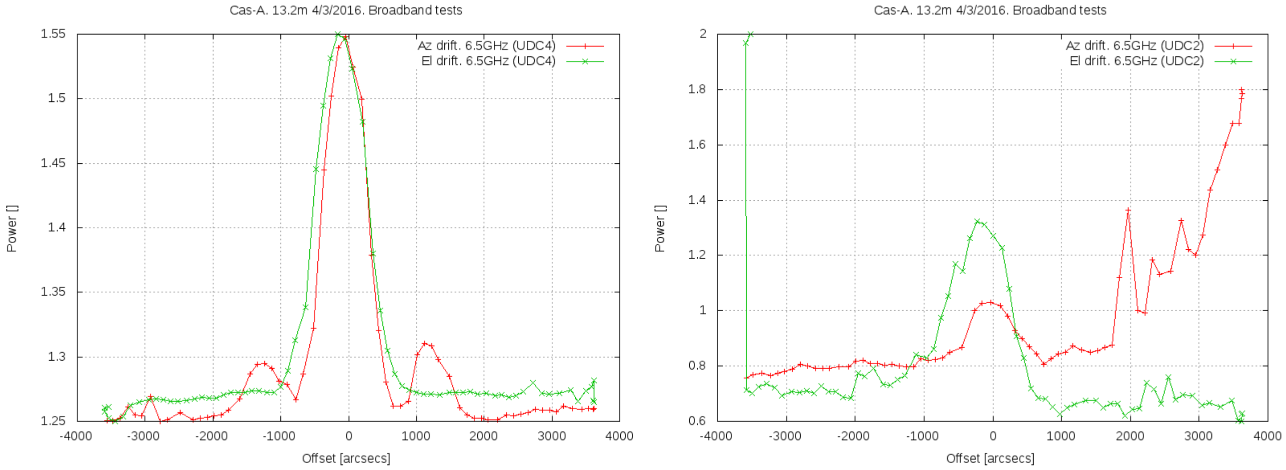

Figure 22: *Pointing drifts at 6.5 GHz towards Cas-A*

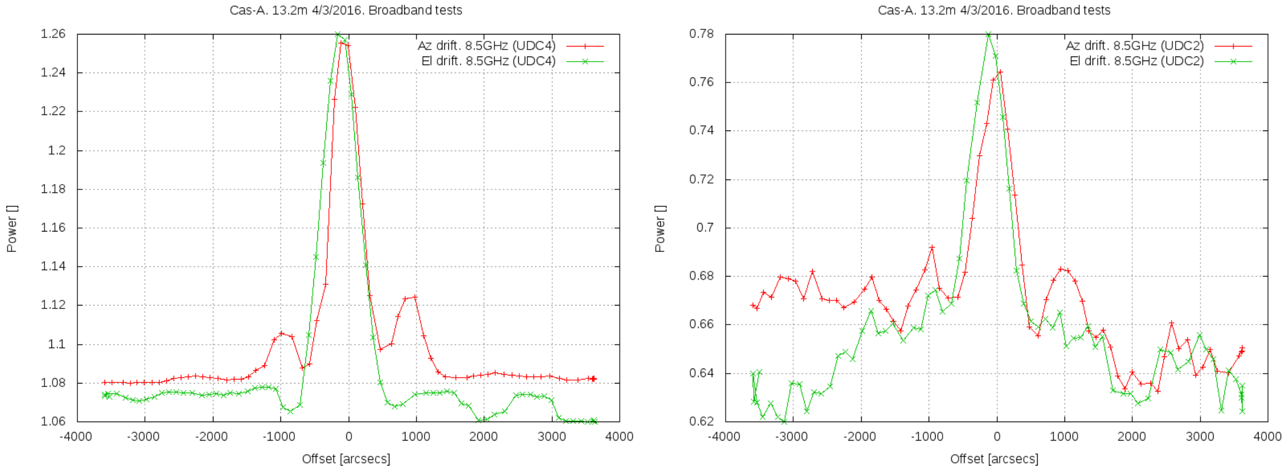

Figure 23: *Pointing drifts at 8.5 GHz towards Cas-A*

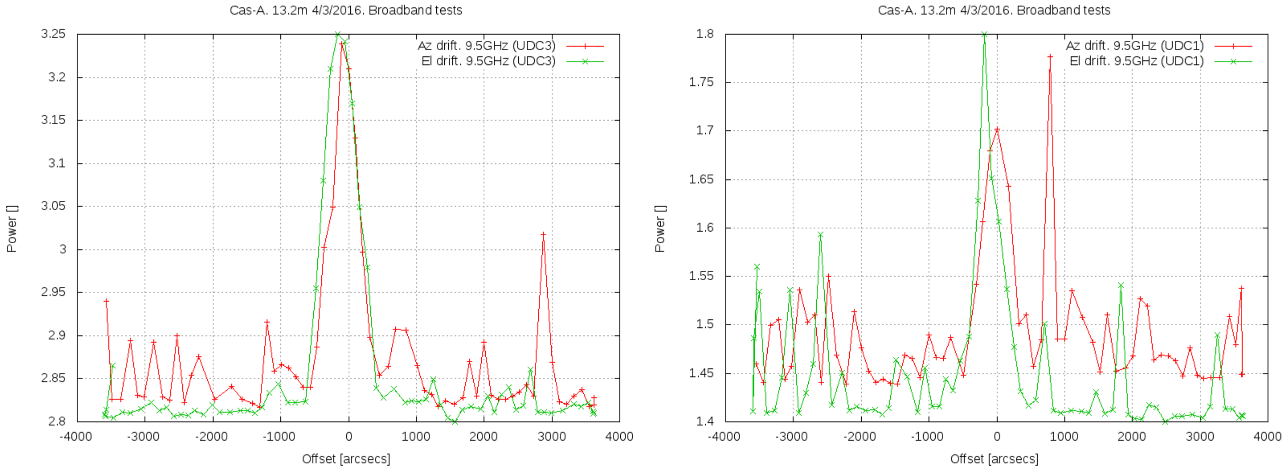

Figure 24: *Pointing drifts at 9.5 GHz towards Cas-A*

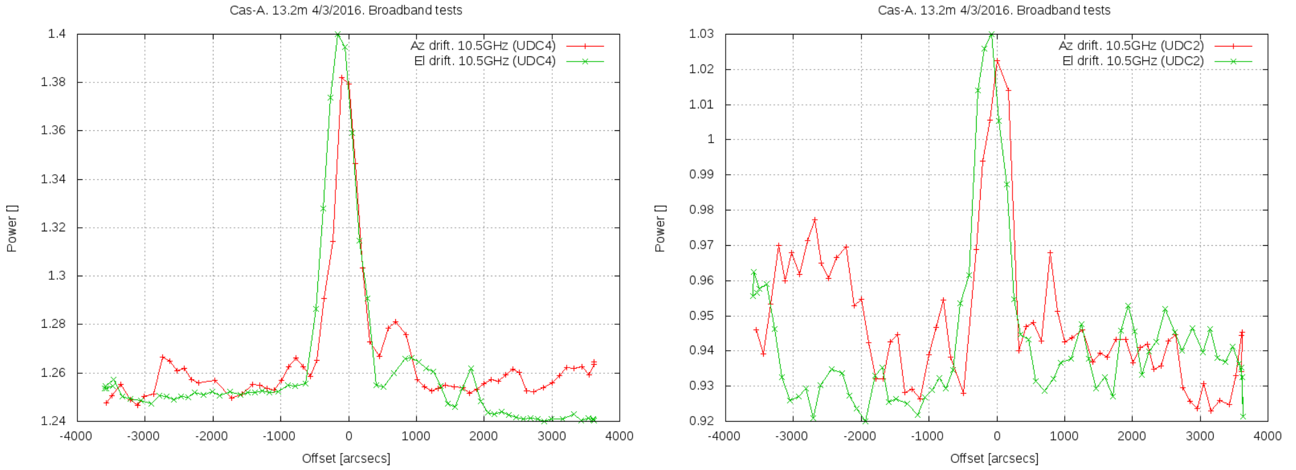

Figure 25: *Pointing drifts at 10.5 GHz towards Cas-A*

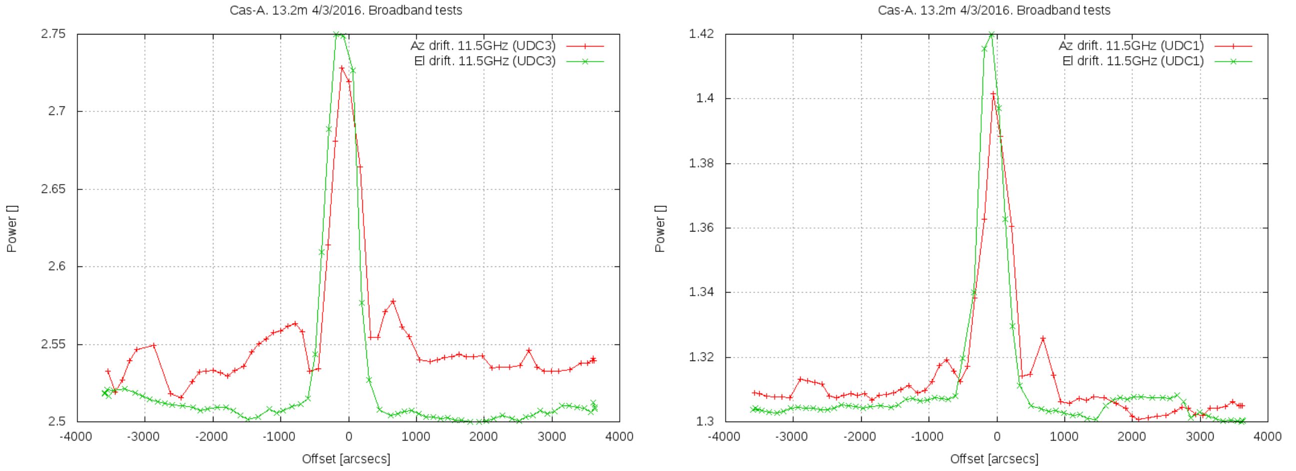

Figure 26: *Pointing drifts at 11.5 GHz towards Cas-A*

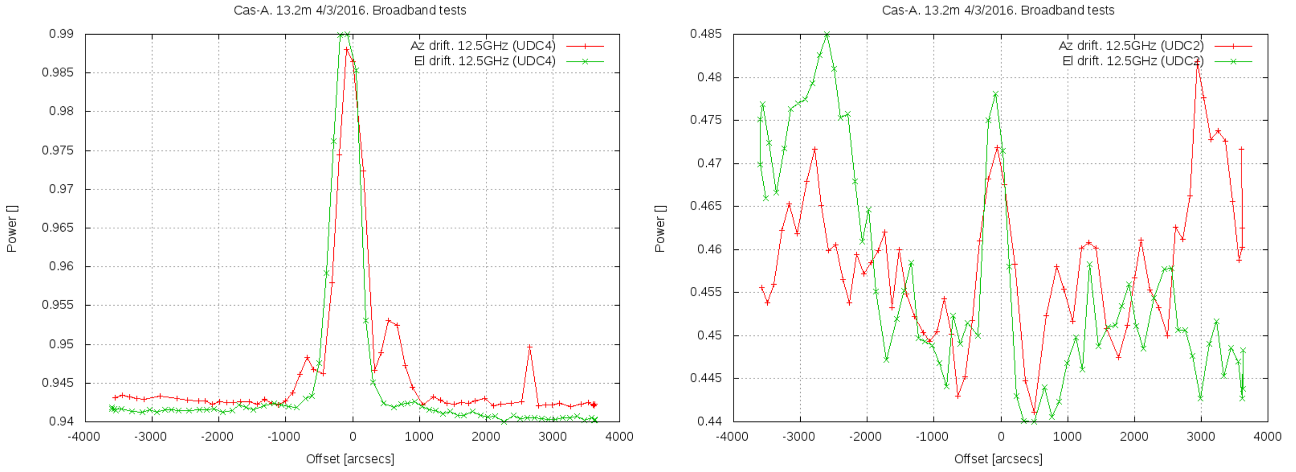

Figure 27: *Pointing drifts at 12.5 GHz towards Cas-A*

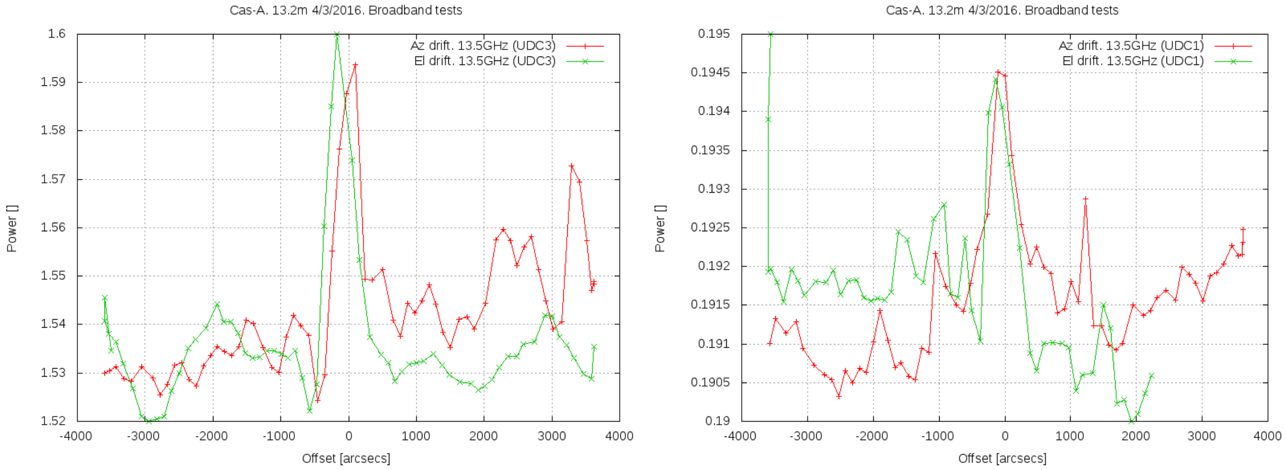

Figure 28: *Pointing drifts at 13.5 GHz towards Cas-A*

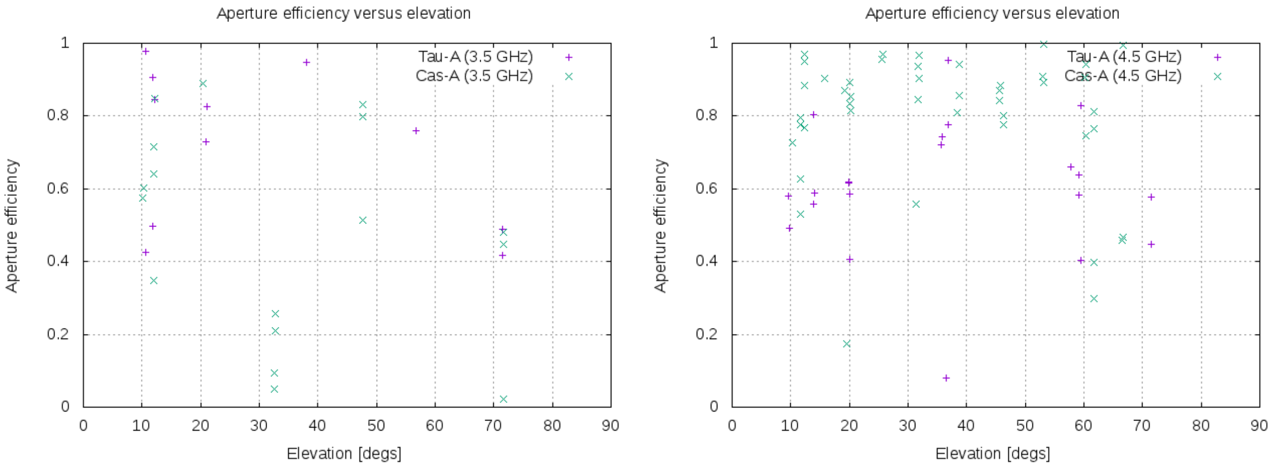

Figure 29: *Gain for 3.5 and 4.5 GHz observing Tau and Cas A using a total power detector with 1 GHz bandwidth.*

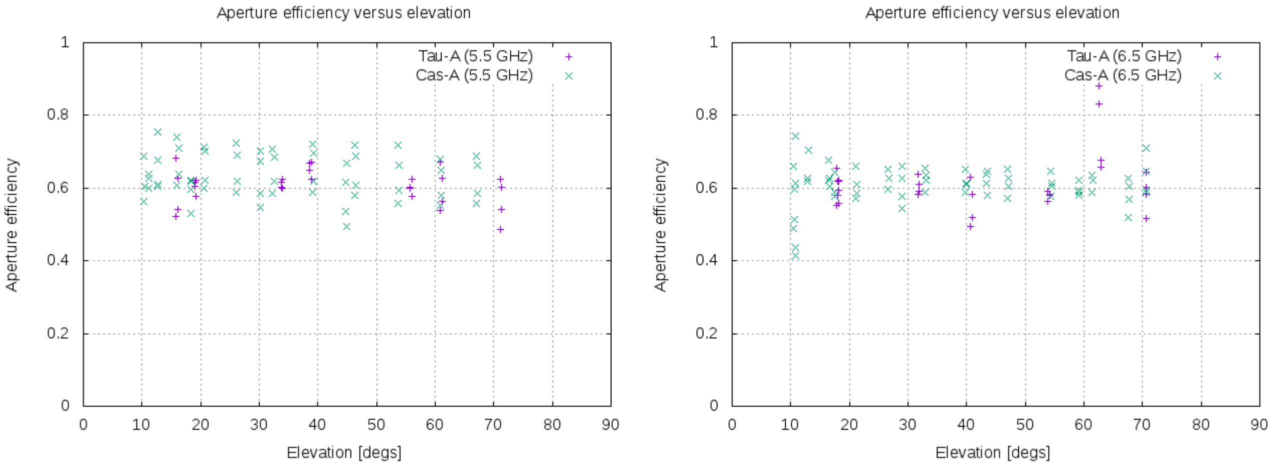

Figure 30: *Gain for 5.5 and 6.5 GHz observing Tau and Cas A using a total power detector with 1 GHz bandwidth.*

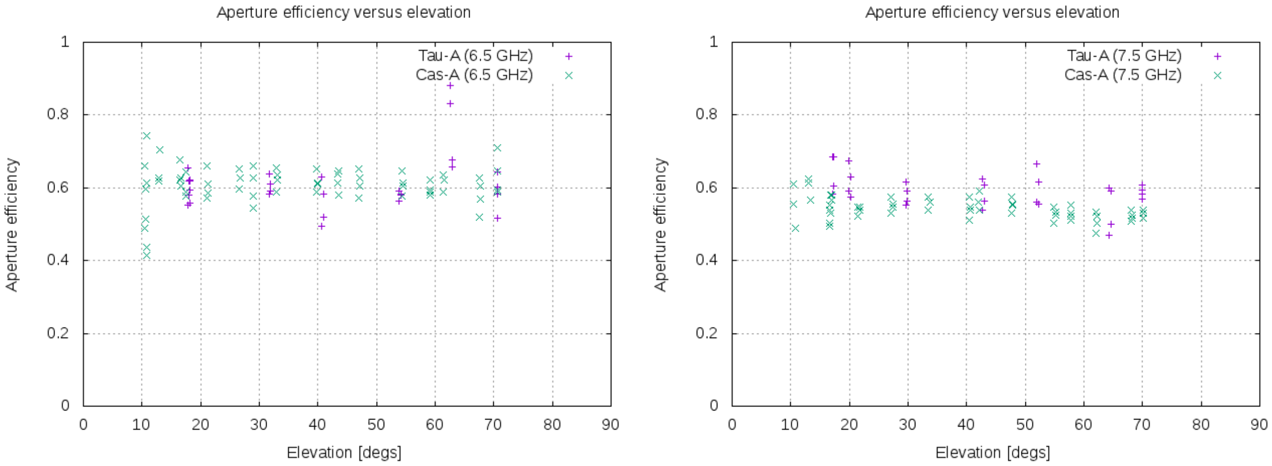

Figure 31: *Gain for 6.5 and 7.5 GHz observing Tau and Cas A using a total power detector with 1 GHz bandwidth.*

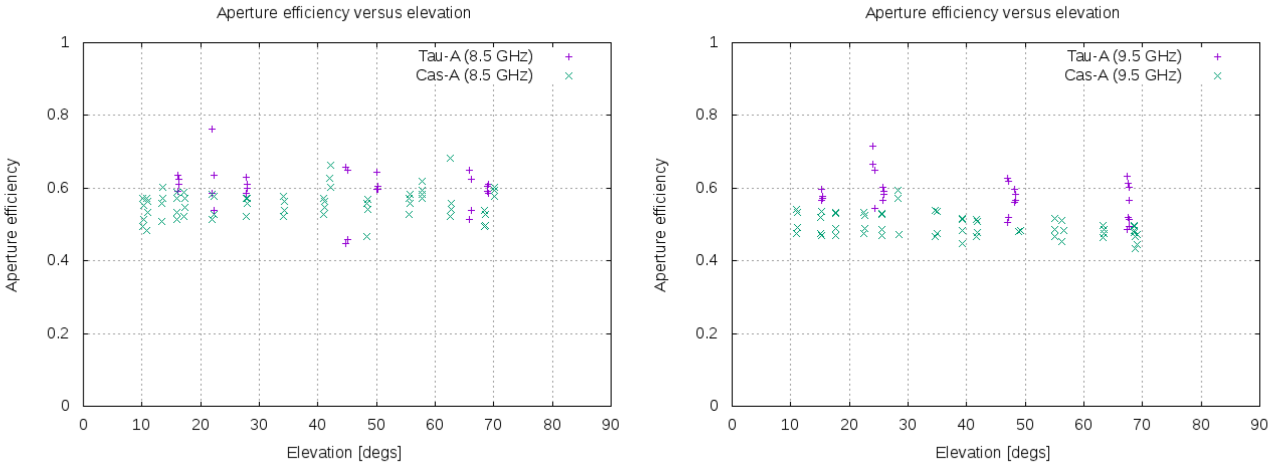

Figure 32: *Gain for 8.5 and 9.5 GHz observing Tau and Cas A using a total power detector with 1 GHz bandwidth.*

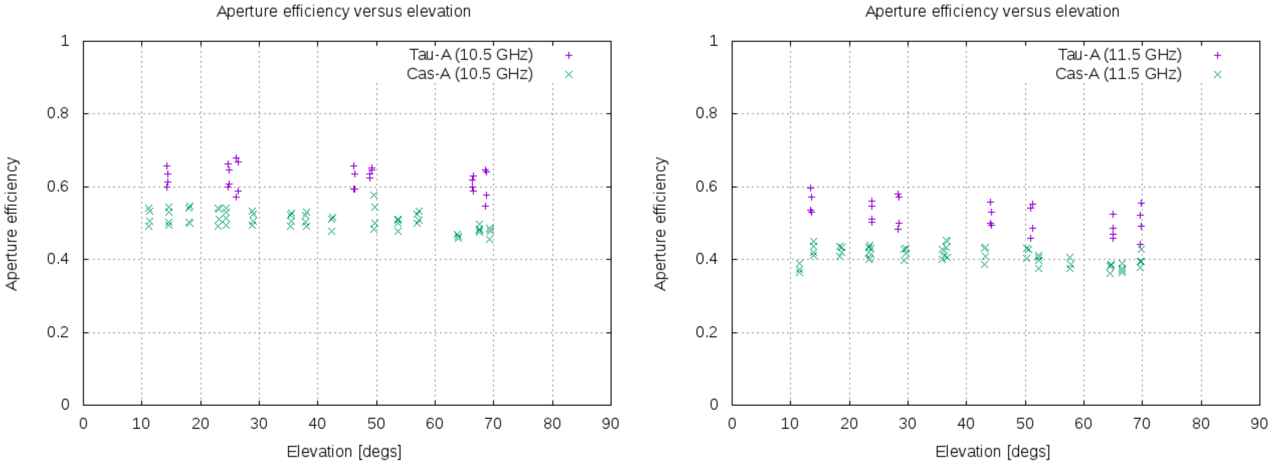

Figure 33: *Gain for 10.5 and 11.5 GHz observing Tau and Cas A using a total power detector with 1 GHz bandwidth.*

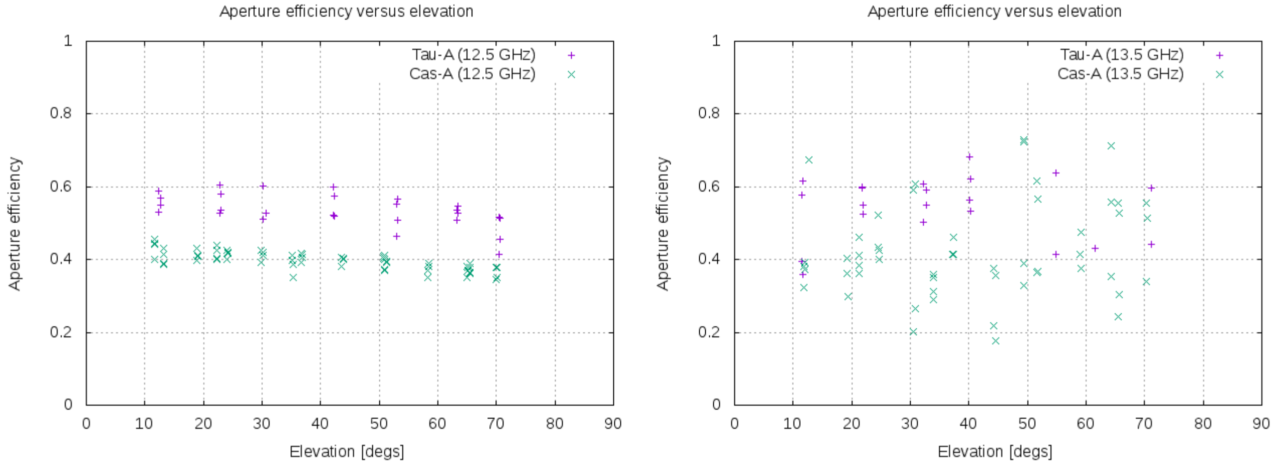

Figure 34: *Gain for 12.5 and 13.5 GHz observing Tau and Cas A using a total power detector with 1 GHz bandwidth.*

[3] Pablo García Carreño, María Patino Esteban, José A. López-Pérez. Medidas del receptor de banda ancha durante su instalación en el radiotelescopio de 13 metros del Observatorio de Yebes. Informe Técnico CDT 2016-4

[4] P. de Vicente. Movimientos de tránsito y seguimiento de planetas con el radiotelescopio de 40m. Informe Técnico OAN 2005-11

[5] Perley R.A.& Butler B.J. Astronomy & Astrophysics Sup. Ser., In preparation. (eprint arXiv:1609.05940) 2016.